Research Square

Preprints are preliminary reports that have not undergone peer review.
They should not be considered conclusive, used to inform clinical practice,
or referenced by the media as validated information.

# Laser-driven gas-phase synthesis of nanodispersed multicomponent oxides for catalytic applications

**Anton I. Kostyukov**

ant.kostyukov@mail.ru

Boreskov Institute of Catalysis SB RAS

**Aleksandr A. Nashivochnikov**

Boreskov Institute of Catalysis SB RAS

**Vladimir N. Snytnikov**

Boreskov Institute of Catalysis SB RAS

**Tamara V. Markelova**

Boreskov Institute of Catalysis SB RAS

**Valeriy N. Snytnikov**

Boreskov Institute of Catalysis SB RAS

**Research Article**

**Keywords:** laser synthesis, laser evaporation, nanomaterials, Al2O3, ZrO2, SiO2, catalysis

**Posted Date:** September 10th, 2026

**DOI:** https://doi.org/10.21203/rs.3.rs-10798531/v1

**License:** This work is licensed under a Creative Commons Attribution 4.0 International License.
Read Full License

**Additional Declarations:** No competing interests reported.

**Version of Record:** A version of this preprint was published at Applied Physics A on November 5th, 2026.
See the published version at https://doi.org/10.1007/s00339-026-10435-2.

# Abstract

Laser-driven gas-phase synthesis provides a powerful route for producing functional oxide nanoparticles with controlled physicochemical properties. However, the formation of multicomponent oxide nanoparticles is strongly affected by differences in the evaporation behavior of the constituent oxides. In this work, we investigate $Al_2O_3$-Cr, $ZrO_2$-Cr, and $SiO_2$-Fe systems as model examples representing three characteristic cases: the effective evaporation temperature of the oxide additive is higher than, close to, or lower than that of the matrix oxide. The nanoparticles were synthesized by laser evaporation of ceramic targets followed by vapor condensation in a controlled argon atmosphere. TEM, HRTEM, HAADF-STEM, EDX mapping, X-ray diffraction, X-ray fluorescence analysis, and BET measurements were used to characterize their morphology, phase composition, elemental distribution, and specific surface area. The results show that the relative evaporation temperatures of the matrix and dopant oxides determine the evaporation sequence, vapor-phase composition, condensation pathway, and ultimately the dopant distribution in the resulting nanoparticles. When the evaporation temperatures are close, homogeneous dopant incorporation is favored, as observed for $ZrO_2$-Cr. In contrast, a large evaporation temperature mismatch leads to sequential evaporation and the formation of composite structures with locally enriched dopant regions, as demonstrated for $Al_2O_3$-Cr and $SiO_2$-Fe. These findings establish a simple criterion for predicting the structure of multicomponent oxide nanoparticles produced by laser gas-phase synthesis and provide a basis for the rational design of catalysts and catalyst supports.


# 1 Introduction

Laser-based material processing is one of the most rapidly developing areas of modern materials science [1–6]. Among these technologies, laser synthesis methods occupy a special place because they provide access to materials for catalysis, optics, ceramics, and biotechnology [5–12].

Laser evaporation in a controlled gaseous environment is of particular interest because it allows the properties of the resulting nanomaterials to be tuned over a wide range [13–15]. At laser intensities below $10^6$ W $cm^{-2}$, evaporation from the surface proceeds without plasma formation, in contrast to laser ablation, and leads to the formation of a boiling melt. By varying the pressure and nature of the ambient gas, as well as the target composition, one can purposefully control both the evaporation process and the characteristics of the final product [16–21]. The productivity of the method is directly related to the laser power and can reach hundreds of grams per hour, opening up prospects for scaling the process for catalytic technologies [22].

The key advantage of laser gas-phase synthesis is the possibility of independently controlling a broad set of physicochemical parameters, including chemical and phase composition, defect structure, mean particle size, specific surface area, and the charge state of dopants in multicomponent oxides. Another important feature of this method is its ability to produce metastable oxide modifications, such as γ-$Al_2O_3$ and the tetragonal and cubic phases of $ZrO_2$, which are widely used as catalyst supports [16–20].

When multicomponent compounds are evaporated, a key feature is the difference in the evaporation rates of the individual components, which is associated with their different boiling temperatures. Despite the broad capabilities of laser gas-phase synthesis for multicomponent oxides, the systematic relationship between the difference in component evaporation temperatures and the formation mechanisms, phase composition, and dopant distribution in nanoparticles remains unclear. This difference can be used for directed synthesis, for example, to obtain $Al_2O_3$-Cr composite catalysts with a reduced toxic $Cr^{6+}$ content, as shown in our previous work [23, 24]. When the evaporation temperatures of the components are close, a more homogeneous dopant distribution in the matrix can be achieved. This represents a classical scenario that is useful for stabilizing the phase composition, for example, the tetragonal and cubic phases of $ZrO_2$ [16–18, 20].

The aim of this work is to establish the specific features of laser gas-phase synthesis of two-component oxide systems. For this purpose, three oxide systems, $Al_2O_3$-Cr, $ZrO_2$-Cr, and $SiO_2$-Fe, were deliberately selected to represent three possible scenarios: the evaporation temperature of the oxide additive is higher than, lower than, or close to that of the matrix component.

The present study demonstrates that the formation mechanism of multicomponent oxide nanoparticles during laser gas-phase synthesis is primarily governed by the relative evaporation temperatures of the matrix and dopant oxides. Three characteristic scenarios are identified and correlated with the resulting nanoparticle morphology, phase composition, and dopant distribution.

# 2 Experimental

## 2.1 Sample characterization

The elemental composition of the nanopowders was determined using an ARL Advant'x X-ray fluorescence (XRF) spectrometer equipped with a Rh anode. The phase composition was studied by X-ray diffraction (XRD) using a Bruker D8 Advance diffractometer with $CuK_\alpha$ radiation ($\lambda$ = 0.15418 nm). Phase identification was performed using the ICDD PDF-2 database. The microstructure and elemental distribution were examined by transmission electron microscopy (TEM) using a Themis-Z 3.1 microscope operated at 200 kV and equipped with an aberration corrector and a Super-X EDS detector. The measurements were carried out in HAADF-STEM mode. Energy-dispersive X-ray (EDX) microanalysis of the elemental composition of the nanopowders was performed using a four-segment Super-X detector in scanning dark-field mode. Elemental distribution maps were acquired by recording characteristic X-ray lines at each point of the analysis region. The specific surface area ($S_{BET}$) was measured by the BET method using low-temperature nitrogen adsorption at 77 K on a DigiSorb-2600 analyzer. Before the measurements, the samples were degassed under vacuum at 200°C for 4 h.

## 2.2 Laser synthesis setup

For laser evaporation, ceramic targets with the compositions α-$Al_2O_3$-Cr, m-$ZrO_2$-Cr, and a-$SiO_2$-Fe containing 5 wt.% Cr or Fe were used. The targets were prepared by uniaxial pressing of micron-sized oxide powders. High-purity analytical-grade $Al_2O_3$, $ZrO_2$, and $SiO_2$ powders served as the starting materials.

Doping with transition-metal elements (Cr and Fe) was performed by incipient wetness impregnation using aqueous solutions of chromium and iron nitrates, followed by drying at 110°C for 4 h and calcination at 550°C for 6 h. After verification of the chemical composition, the powders were compacted by uniaxial pressing at a pressure of at least 15 MPa. The resulting pellets were subsequently sintered in air at 1250°C for 6 h.

Nanopowders were synthesized by laser evaporation using a two-chamber reactor described in detail elsewhere [16]. A ceramic target of the required composition was placed in a crucible inside a sealed evaporation chamber. Evaporation was performed using focused radiation from a cw $CO_2$ laser with an output power of 100 W. The laser beam was focused into a spot with a diameter of 0.4–0.5 mm, producing a local boiling zone on the target surface with a molten pool approximately 2–3 mm in diameter. The temperature in the evaporation zone corresponded to the boiling temperature of the oxide under the given pressure conditions. A schematic diagram of the experimental setup is shown in Fig. 1b. Figure 1a additionally provides a schematic representation of nanoparticle formation during laser evaporation, highlighting the main physical processes, including laser-induced boiling of the target, vapor expansion, nucleation, condensation, and particle growth.

The generated vapor and fine fragments were entrained by the buffer gas flow and passed through a labyrinth separator, which efficiently removed large droplets and molten splashes before entering the deposition zone. The presence of the buffer gas reduced the kinetic energy of the vapor species, thereby promoting nucleation and nanoparticle growth.

Cooling and condensation of the evaporated material occurred in a flow of high-purity argon (99.999%). For all samples investigated in this work, evaporation was carried out at a pressure of 0.1 atm. The chamber pressure served as the primary parameter controlling the particle size and was maintained constant throughout the synthesis.

This pressure was intentionally selected because it yields nanoparticles with an average size of approximately 10 nm. Such particle dimensions enable reliable visualization of compositional inhomogeneity and phase separation by TEM imaging and EDX elemental mapping. The synthesized nanopowder was collected on ash-free paper filters and subsequently characterized using conventional physicochemical techniques.

# 3 Results and discussion

Laser evaporation enables the synthesis of a broad variety of functional oxide nanomaterials consisting of weakly agglomerated nanoparticles. One of the major advantages of this technique is the ability to

control the particle size over a wide range, from approximately 2 to more than 50 nm, which directly determines the specific surface area of the resulting powders. The oxide nanopowders produced by this method exhibit a highly developed specific surface area, which is one of the key parameters governing their catalytic performance. For example, alumina nanoparticles with a diameter of 4–5 nm exhibit a BET surface area of approximately 360 $m^2 g^{-1}$. For zirconia nanoparticles with a size of 2–3 nm, the specific surface area reaches about 300 $m^2 g^{-1}$, whereas silica nanoparticles of comparable size possess a BET surface area of approximately 200 $m^2 g^{-1}$. Since the catalytic activity of heterogeneous catalysts is directly proportional to the number of accessible active sites, the capability of producing nearly monodisperse nanoparticles with controllable size and high specific surface area represents a significant advantage of laser gas-phase synthesis. The established relationship between the synthesis conditions and particle size therefore provides an effective route for tailoring catalyst and catalyst-support properties.

Another important advantage of laser synthesis is the possibility of controlling the composition of the surrounding gas atmosphere, thereby enabling synthesis under well-defined oxidation-reduction conditions. This makes it possible to control the oxidation state of catalytically active species, which is important both for fundamental studies of active centers and for the development of multicomponent catalysts based on transition-metal oxides with improved catalytic performance.

The evaporation of refractory oxides is generally a complex, non-congruent process involving multiple gaseous species. In multicomponent systems, differences in the evaporation behavior of the constituent oxides additionally affect the composition and temporal evolution of the vapor phase. However, unlike single-component oxides, the laser synthesis of multicomponent systems is associated with several additional technological challenges. The primary reason is the difference in the evaporation temperatures of the constituent oxides. This feature must be taken into account in several important aspects.

First, differences in the evaporation temperatures of the individual components lead to deviations of the chemical composition of the synthesized nanopowders from that of the initial target. To compensate for this effect, preliminary optimization of the target composition is required in order to obtain nanopowders with the desired stoichiometry. This procedure becomes particularly important when comparing the functional properties, especially the catalytic performance, of materials prepared by different synthesis methods. An alternative approach is the complete evaporation of the ceramic target. However, this strategy increases the risk of laser interaction with the crucible bottom, which may result in contamination of the synthesized material.

A second technological issue becomes particularly pronounced when the boiling temperatures of the constituent oxides differ significantly. Under these conditions, the component with the lower boiling temperature evaporates more rapidly than the refractory component. Consequently, the composition of the vapor phase changes continuously during synthesis, leading to temporal variations in the composition of the synthesized nanopowder. Such behavior complicates the preparation of reproducible

samples for comparative studies. Although this problem can, in principle, be addressed by dynamically adjusting the target composition during synthesis, such an approach is technically demanding and requires extensive preliminary optimization. Our systematic studies have shown that reproducibility can be substantially improved by maintaining identical evaporation times for all samples or by completely evaporating the target.

Finally, large differences in evaporation temperatures hinder the formation of a homogeneous solid solution. Instead, the target nanomaterial often forms a composite structure in which phases of the individual components coexist separately.

After laser evaporation, the phase composition of the investigated materials undergoes substantial transformation. For the α-$Al_2O_3$-Cr and m-$ZrO_2$-Cr systems, a transition to the metastable oxide phases γ-$Al_2O_3$-Cr and t-$ZrO_2$-Cr, respectively, is observed. In the case of a-$SiO_2$-Fe, the amorphous structure of $SiO_2$ is retained. It is important to note that changes in the lattice parameters of multicomponent oxides were detected only for the t-$ZrO_2$-Cr sample, indicating isomorphic incorporation of chromium (dopant) into the zirconia lattice (matrix). This effect is associated with the difference in the boiling/evaporation temperatures of the components and is discussed below based on TEM and EDX data. Experimental studies on the laser synthesis of various oxide compounds have revealed that when the target is irradiated with moderate-power laser radiation (an order of magnitude lower than that required for the actual evaporation process), the target surface begins to melt, and already at this stage evaporation of material from the surface occurs, as evidenced by the detection of nanoparticles on the filter. Consequently, in principle, only the boiling temperature may be further employed as an initial criterion for analyzing the evaporation behaviour of multicomponent oxides. For comparison, the characteristic boiling temperatures reported at atmospheric pressure were used as a thermodynamic reference for evaluating the relative volatility of the constituent oxides. Figures 2 and 3 show TEM, HRTEM, HAADF-STEM, and EDX elemental maps for chromium distribution in $Al_2O_3$-Cr and $ZrO_2$-Cr nanopowders.

According to TEM observations, the $Al_2O_3$-Cr and $ZrO_2$-Cr nanopowders obtained by laser evaporation consist of weakly agglomerated, nearly spherical particles with a narrow size distribution. For $Al_2O_3$-Cr, the average particle diameter is approximately 15 nm. The particles are highly crystalline and predominantly correspond to the low-temperature γ-$Al_2O_3$ modification. For $ZrO_2$-Cr, the average particle size is about 10 nm; the particles are also highly crystalline and mainly correspond to the t-$ZrO_2$ phase. The BET specific surface area is approximately 130 $m^2\ g^{-1}$ for $Al_2O_3$-Cr and approximately 100 $m^2\ g^{-1}$ for $ZrO_2$-Cr, which is consistent with the particle sizes estimated from TEM images.

The EDX elemental maps reveal a distinct difference in chromium distribution between the $Al_2O_3$-Cr and $ZrO_2$-Cr systems. In both cases, chromium ions are distributed throughout the sample volume. However, in the $Al_2O_3$-Cr system, local regions with an increased dopant concentration are clearly observed, whereas in $ZrO_2$-Cr chromium is distributed more homogeneously over the entire oxide matrix. This difference originates from the mismatch between the evaporation temperatures of the oxides forming

the solid-solution targets. In the $Al_2O_3$-Cr system, the evaporation temperature of α-$Cr_2O_3$ (approximately 4000°C at 1 atm) is substantially higher than that of α-$Al_2O_3$ (approximately 3000°C at 1 atm). As a result, the more volatile matrix oxide, alumina, evaporates preferentially at the initial stage of laser synthesis. After chromium becomes enriched in the evaporation zone, evaporation of residual $Cr_2O_3$ begins to dominate. This sequential evaporation mechanism leads to the formation of a composite $Al_2O_3$-$Cr_2O_3$ structure rather than a homogeneous solid solution, producing a nonuniform chromium distribution. In the $ZrO_2$-Cr system, the evaporation temperatures of the components are much closer, with $ZrO_2$ evaporating at approximately 4300°C (at 1 atm). This similarity enables more synchronous evaporation of both oxides, thereby preserving the homogeneity of the solid solution and promoting a uniform dopant distribution within the nanoparticles.

A separate case is represented by multicomponent oxides in which the evaporation or boiling temperature of the oxide additive is lower than that of the matrix. One example studied in this work is the $SiO_2$-Fe binary oxide system. In contrast to $Al_2O_3$-Cr and $ZrO_2$-Cr, the $SiO_2$-Fe samples synthesized by laser evaporation exhibit distinct morphological features. TEM data show that the $SiO_2$-based particles are significantly more agglomerated and form large micron- and submicron-sized blocks. Within these blocks, high-resolution TEM images reveal individual particles with an average size of approximately 10 nm. The specific surface area of these particles is approximately 100 $m^2\ g^{-1}$, which is substantially lower than the value expected for isolated spherical particles of the same size. This discrepancy is attributed to stronger nanoparticle agglomeration.

Figure 4 presents the EDX elemental mapping results for $SiO_2$-Fe nanoparticles obtained by laser evaporation. According to reference data, the boiling temperature of α-$Fe_2O_3$ is approximately 1990°C; however, under laser evaporation conditions it may decompose with the formation of $Fe_3O_4$ and FeO [21]. Literature values for the boiling point of $SiO_2$ span from ~ 2200°C to ~ 2900°C [25]. Thus, the evaporation or decomposition temperature of the iron-containing phase is substantially lower than that of the silica matrix. Consequently, during laser synthesis, vapor of iron-containing species ($Fe_xO_y$) is generated first. During nucleation, this vapor condenses preferentially, forming nanosized particles or locally enriched regions. $SiO_2$ vapor then condenses on or around these regions. This sequential mechanism results in local enrichment of iron in certain areas of the sample, which is clearly observed in the EDX maps in Fig. 4.

The comparison of $Al_2O_3$-Cr, $ZrO_2$-Cr, and $SiO_2$-Fe demonstrates that the relative evaporation temperatures of the matrix and oxide additive act as a governing parameter in laser gas-phase synthesis. This parameter determines the evaporation sequence, the temporal evolution of the vapor composition, the condensation pathway, and ultimately the spatial distribution of dopants in the synthesized nanoparticles, as shown in Fig. 5. These trends are not limited to chromium and iron additives. Similar behavior has been observed for Cr, Mn, Fe, Eu, and Tb oxides in an $Al_2O_3$ matrix, for Cr, Fe oxides in an $SiO_2$ matrix, for Cr, Eu, Ln, and Y oxides in $ZrO_2$, and for binary rare-earth oxide systems. Therefore, the

evaporation-temperature relationship can be considered a practical criterion for predicting the formation pathway of multicomponent oxide nanoparticles during laser gas-phase synthesis.

This capability is particularly attractive for catalysis, as it provides a route to controlling dopant distribution, be it homogeneous, matrix-enriched, or dopant-enriched, directly influencing metal–support interactions, active site accessibility, and thermal stability. Hence, the evaporation-temperature criterion provides a straightforward guideline for the rational design of catalysts, supports, and functional oxide materials.

# 4 Conclusions

This work establishes a general criterion governing the laser gas-phase synthesis of multicomponent oxide nanoparticles. The relative evaporation temperatures of the matrix and dopant oxides determine the evaporation sequence, vapor-phase composition, condensation mechanism, and ultimately the spatial distribution of dopants in the synthesized nanoparticles. Three characteristic synthesis scenarios were identified.

First, when the evaporation temperature of the oxide additive is substantially higher than that of the matrix, as in $Al_2O_3$-Cr and related systems, evaporation proceeds sequentially: the matrix evaporates first, followed by the refractory dopant oxide. This pathway leads to composite nanoparticles with nonuniform dopant distribution and local dopant-enriched regions. Such materials may be promising for catalytic applications, as previously shown for $Al_2O_3$-Cr systems.

Second, when the evaporation temperatures of the matrix and oxide additive are close, as in $ZrO_2$-Cr, evaporation proceeds more synchronously. This favors homogeneous dopant incorporation and the formation of nanoparticles with a more uniform elemental distribution. Such systems are particularly relevant for catalyst supports as well as for optical and ceramic technologies that require phase stabilization and compositional homogeneity.

Third, when the evaporation temperature of the oxide additive is lower than that of the matrix, as in $SiO_2$-Fe, the additive evaporates first and the matrix subsequently condenses on or around the initially formed dopant-containing species. This also results in composite structures with nonuniform elemental distribution.

Overall, the proposed evaporation-temperature criterion provides a simple and physically transparent design principle for selecting multicomponent oxide systems suitable for laser gas-phase synthesis. Under comparable laser gas-phase synthesis conditions, this criterion can be used to anticipate whether a given oxide combination will favor homogeneous solid-solution-like nanoparticles or composite structures with locally enriched dopant regions.

# Declarations

# Funding

This work was supported by the Ministry of Science and Higher Education of the Russian Federation within the state assignment of the Boreskov Institute of Catalysis SB RAS (project FWUR-2024-0033).

# Author Contribution

A.I.K., V.N. Snytnikov (Vladimir), and V.N. Snytnikov (Valeriy) conceived and designed the study. A.I.K., A.A.N., and V.N. Snytnikov (Vladimir) conducted the experimental work. A.I.K., T.V.M., and A.A.N. performed the data analysis and interpretation. All authors discussed the results and contributed to the writing, review, and editing of the manuscript. All authors read and approved the final version.

# Acknowledgement

The authors are grateful to A.V. Ishchenko, PhD, for TEM measurements, S.V. Cherepanova, PhD, for XRD analysis, and A.B. Ayupov for specific surface area measurements. Sample characterization was performed using the equipment of the National Center for Catalyst Research.

# Data Availability

Raw datasets (XRD patterns, XRF spectra, and BET isotherms) are available from the corresponding author on reasonable request.

## References

1. A. A. Manshina, I. I. Tumkin, E. M. Khairullina, M. Mizoshiri, A. Ostendorf, S. A. Kulinich, S. Makarov, A. A. Kuchmizhak, E. L. Gurevich, The second laser revolution in chemistry: emerging laser technologies for precise fabrication of multifunctional nanomaterials and nanostructures. Adv. Funct. Mater. **34**, 2405457 (2024). https://doi.org/10.1002/adfm.202405457.
2. Y. Liu, J. Yuan, J. Zhou, et al., Laser solid-phase synthesis of graphene shell-encapsulated high-entropy alloy nanoparticles. Light Sci. Appl. **13**, 270 (2024). https://doi.org/10.1038/s41377-024-01614-y.
3. L. Yang, J. Wei, Z. Ma, P. Song, J. Ma, Y. Zhao, Z. Huang, M. Zhang, F. Yang, X. Wang, The Fabrication of Micro/Nano Structures by Laser Machining. Nanomaterials **9**(12), 1789 (2019). https://doi.org/10.3390/nano9121789.
4. M. B. Larosi, J.d.V.García, A.R. Rodríguez, Laser Synthesis of Nanomaterials. Nanomaterials **12**(17), 2903 (2022). https://doi.org/10.3390/nano12172903.

5. N. Luo, C. Yang, X. Tian, J. Xiao, J. Liu, F. Chen, D. Zhang, D. Xu, Y. Zhang, G. Yang, D. Chen, L. Li, A general top-down approach to synthesize rare earth doped-$Gd_2O_3$ nanocrystals as dualmodal contrast agents. J. Mater. Chem. B **2**(35):5891–5897 (2014). https://doi.org/10.1039/c4tb00695j.
6. M. A. Zakaria, M. Abdelraof, R. H. El-Gebaly, et al. Laser-assisted method for preparation of nanocomposites based on magnetite and noble metals for biomedical applications. Appl. Phys. A **130**, 132 (2024). https://doi.org/10.1007/s00339-024-07283-3.
7. M. Shi, Y. Kitamoto, M. Hara, et al. Preparation of $CeO_2$ nanoparticles by laser ablation in liquid method and its UV-absorption properties. Appl. Phys. A **128**, 968 (2022). https://doi.org/10.1007/s00339-022-06086-8.
8. P. Segovia-Olvera, N. Ramos-Camacho, A. Esparza-Garcia, et al. Vanadium dioxide ($VO_2$) nanostructure formation and gradient patterning on vanadium films via femtosecond laser processing. Appl. Phys. A 131, 811 (2025). https://doi.org/10.1007/s00339-025-08906-z.
9. A. Toulil, E. Kachan, Y. G. Yingling, et al. Oxidation and laser synthesis of Ni nanoparticles: an atomistic analysis. Appl. Phys. A 131, 916 (2025). https://doi.org/10.1007/s00339-025-09047-z.
10. V. V. Osipov, A. V. Ishchenko, V. A. Shitov, R. N. Maksimov, K. E. Lukyashin, V. V. Platonov, A. N. Orlov, S. N. Osipov, V. V. Yagodin, L. V. Viktorov, B. V. Shulgin, Fabrication, optical and scintillation properties of transparent YAG:Ce ceramics. Optical Materials **71**, 98–102 (2017). https://doi.org/10.1016/j.optmat.2016.05.016.
11. U. Lohbauer, A. Wagner, R. Belli, C. Stoetzel, A. Hilpert, H.-D. Kurland, J. Grabow, F.A. Müller, Zirconia nanoparticles prepared by laser vaporization as fillers for dental adhesives. Acta Biomaterialia **6**(12), 4539–4546 (2010). https://doi.org/10.1016/j.actbio.2010.07.002.
12. J. Häusler, F. A. Müller, L. Müller, J. Grabow, C. Cleve, C. Lotz, M. Röschlau, P. Bittorf, R. Fromme, I. Kiebert, M. Grüne, S. Schweizer, and S. Dembski, Preparation of phosphorescent $Eu^{2+}$, $Dy^{3+}$-doped strontium aluminate nanoparticles by laser vaporization for the modification of therapeutic contact lenses. Adv. Photonics Res. **3**, 2200013 (2022). https://doi.org/10.1002/adpr.202200013.
13. N. Abid, A. M. Khan, S. Shujait, K. Chaudhary, M. Ikram, M. Imran, J. Haider, M. Khan, Q. Khan, M. Maqbool, Synthesis of nanomaterials using various top-down and bottom-up approaches, influencing factors, advantages, and disadvantages: A review. Advances in Colloid and Interface Science **300**, 102597 (2022). https://doi.org/10.1016/j.cis.2021.102597.
14. N. Baig, I. Kammakakam, W. Falath, Nanomaterials: a review of synthesis methods, properties, recent progress, and challenges. Mater. Adv. **2**(6), 1821–1871 (2021). https://doi.org/10.1039/d0ma00807a.
15. M. Malekzadeh, M. T. Swihart, Vapor-phase production of nanomaterials. Chem. Soc. Rev. **50** (12), 7132–7249 (2021). https://doi.org/10.1039/d0cs01212b.
16. A. I. Kostyukov, T. V. Markelova, A. A. Nashivochnikov, V. N. Snytnikov, E. A. Suprun, V. N. Snytnikov, Laser synthesis of oxide nanoparticles with controlled gas condensation. Journal of Aerosol Science **181**, 106434:1–12 (2024). https://doi.org/10.1016/j.jaerosci.2024.106434.

17. B. Osswald, L. Müller, J. Grabow, F. A. Müller, F. Kern, Evaluation of 1.5 mol% yttria – 1.5 mol% gadolinia stabilized tetragonal zirconia polycrystals derived from solid state synthesis and laser vaporation. Journal of the European Ceramic Society **45**(10), 117345 (2025). https://doi.org/10.1016/j.jeurceramsoc.2025.117345.
18. H.-D. Kurland, J. Grabow, F. A. Müller, Preparation of ceramic nanospheres by $CO_2$ laser vaporization (LAVA). Journal of the European Ceramic Society **31**(14), 2559–2568 (2011). https://doi.org/10.1016/j.jeurceramsoc.2011.01.010.
19. A. I. Kostyukov, V. N. Snytnikov, A. V. Zhuzhgov, S. V. Cherepanova, A. V. Ishchenko, M. G. Baronskiy, V. N. Snytnikov, Size-dependent photoluminescence of europium in alumina nanoparticles synthesized by cw $CO_2$ laser vaporization. Journal of Alloys and Compounds **815**, 152476:1–12 (2020). https://doi.org/10.1016/j.jallcom.2019.152476.
20. A. A. Nashivochnikov, A. I. Kostyukov, M. I. Rakhmanova, V. N. Panchenko, S. V. Cherepanova, V. N. Snytnikov, Particle size effect on the structure, morphology and optical properties of europium doped $ZrO_2$ nanoparticles. Ceramics International **49**(24 Part A), 40051–40060 (2023). https://doi.org/10.1016/j.ceramint.2023.09.335.
21. V. V. Osipov, V. V. Platonov, M. A. Uimin, et al. Laser synthesis of magnetic iron oxide nanopowders. Tech. Phys. **57**, 543–549 (2012). https://doi.org/10.1134/S1063784212040214.
22. U. Popp, R. Herbig, G. Michel, E. Müller, Ch. Oestreich, Properties of nanocrystalline ceramic powders prepared by laser evaporation and recondensation. Journal of the European Ceramic Society **18** (9), 1153–1160 (1998). https://doi.org/10.1016/S0955-2219(98)00037-5.
23. A. I. Kostyukov, N. A. Zaitseva, A. A. Nashivochnikov, A. V. Zhuzhgov, V. V. Kaichev, V. V. Kriventsov, V. N. Snytnikov, Dehydrogenation activity of $Cr^{6+}$ free laser-synthesized $Cr_2O_3$–$Al_2O_3$ nanocomposite catalysts. Materials Today Chemistry **42**, 102458:1–10 (2024). https://doi.org/10.1016/j.mtchem.2024.102458.
24. A. I. Kostyukov, M. G. Baronskiy, T. V. Larina, V. N. Snytnikov, N. A. Zaitseva, A. A. Pochtar, A. V. Ishchenko, S. V. Cherepanova, V. N. Snytnikov, Laser vaporized $CrO_x/Al_2O_3$ nanopowders as a catalyst for isobutane dehydrogenation. Materials Characterization **169**, 110664–110678 (2020). https://doi.org/10.1016/j.matchar.2020.110664.
25. R. G. Kraus, S. T. Stewart, D. C. Swift, C. A. Bolme, R. F. Smith, S. Hamel, B. D. Hammel, D. K. Spaulding, D. G. Hicks, J. H. Eggert,G. W. Collins, events, Shock vaporization of silica and the thermodynamics of planetary impact events. J. Geophys. Res.**117**, E09009 (2012) https://doi.org/10.1029/2012JE004082.

# Figures

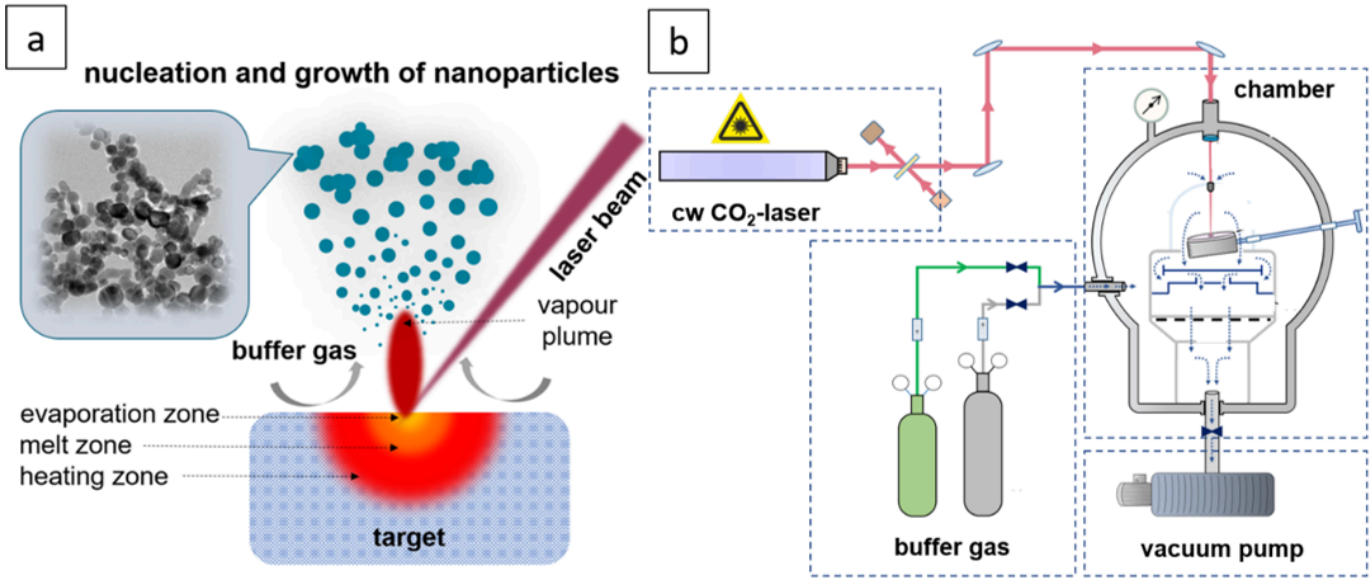



**Figure 1**

Illustration of the laser evaporation system: (a) schematic representation of nanoparticle formation during laser evaporation; (b) experimental setup. Arrows indicate the direction of gas flow.

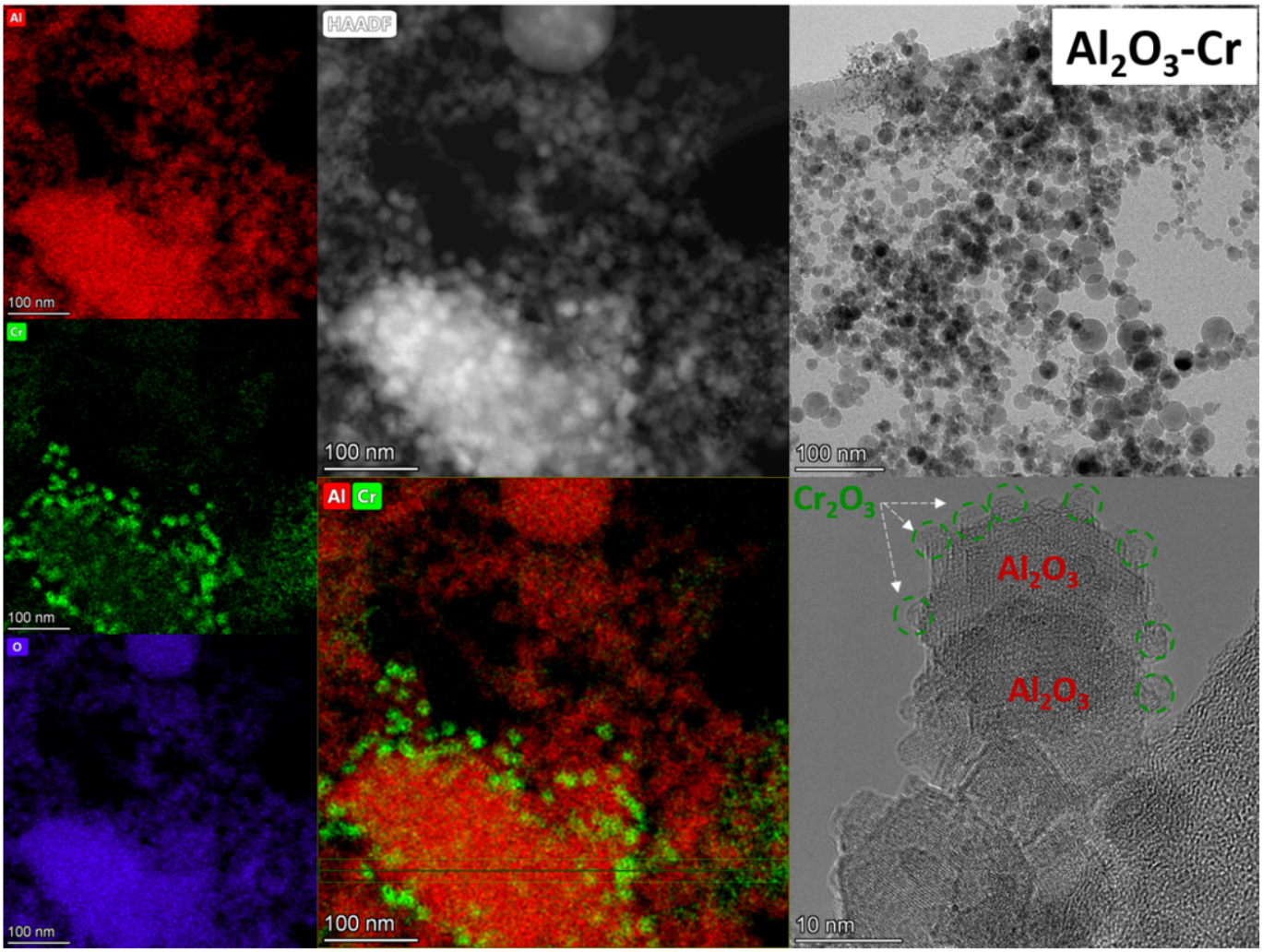


**Figure 2**

TEM, HRTEM, and HAADF-STEM images of $Al_2O_3$-Cr nanoparticles with EDX elemental maps of Al (red), Cr (green), and O (violet). For clarity, the most representative HRTEM image from our previous work [**23**] is shown to illustrate the observed effect.

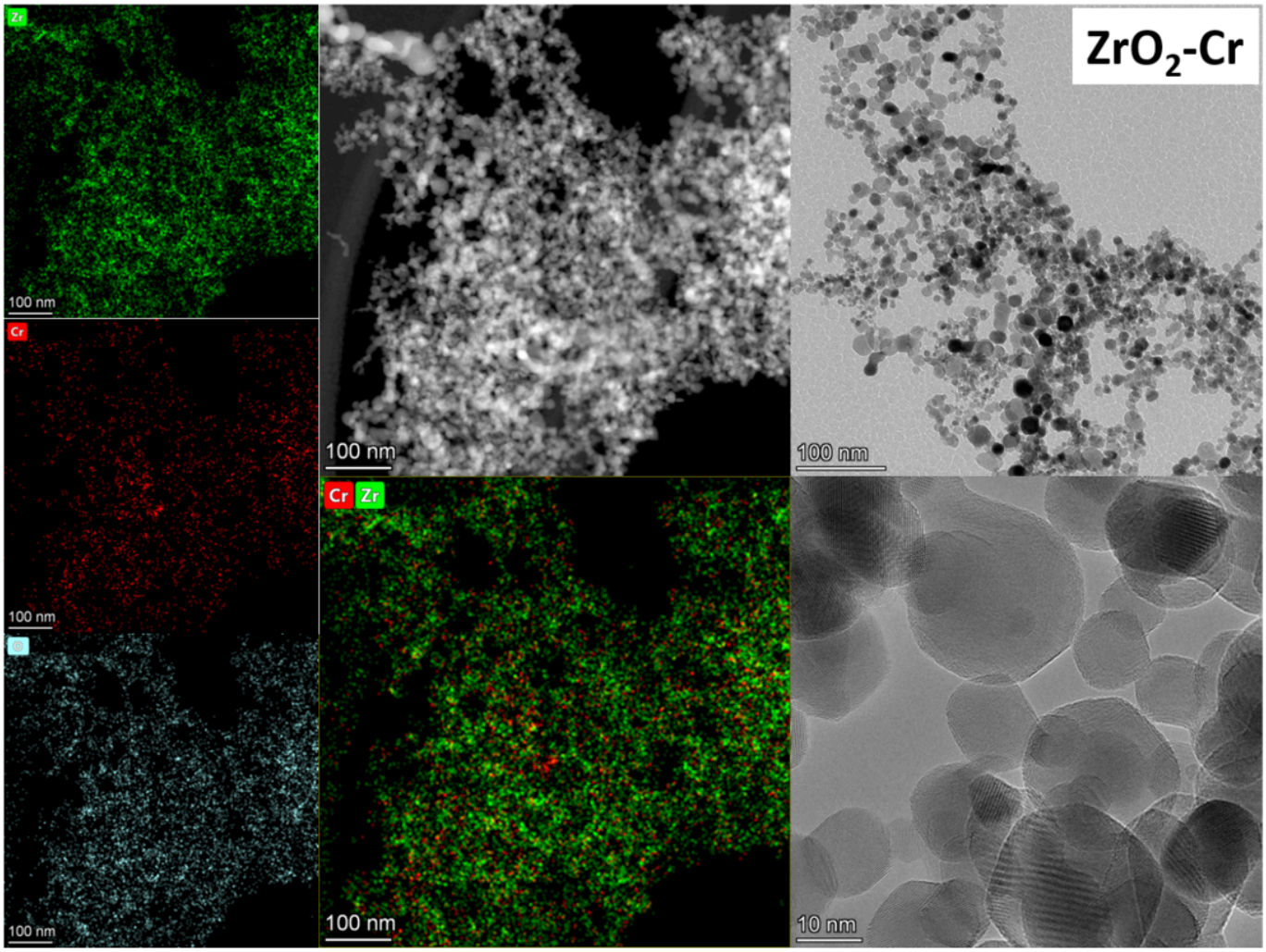



**Figure 3**

TEM, HRTEM, and HAADF-STEM images of $ZrO_2$-Cr nanoparticles with EDX elemental maps of Zr (green), Cr (red), and O (blue).

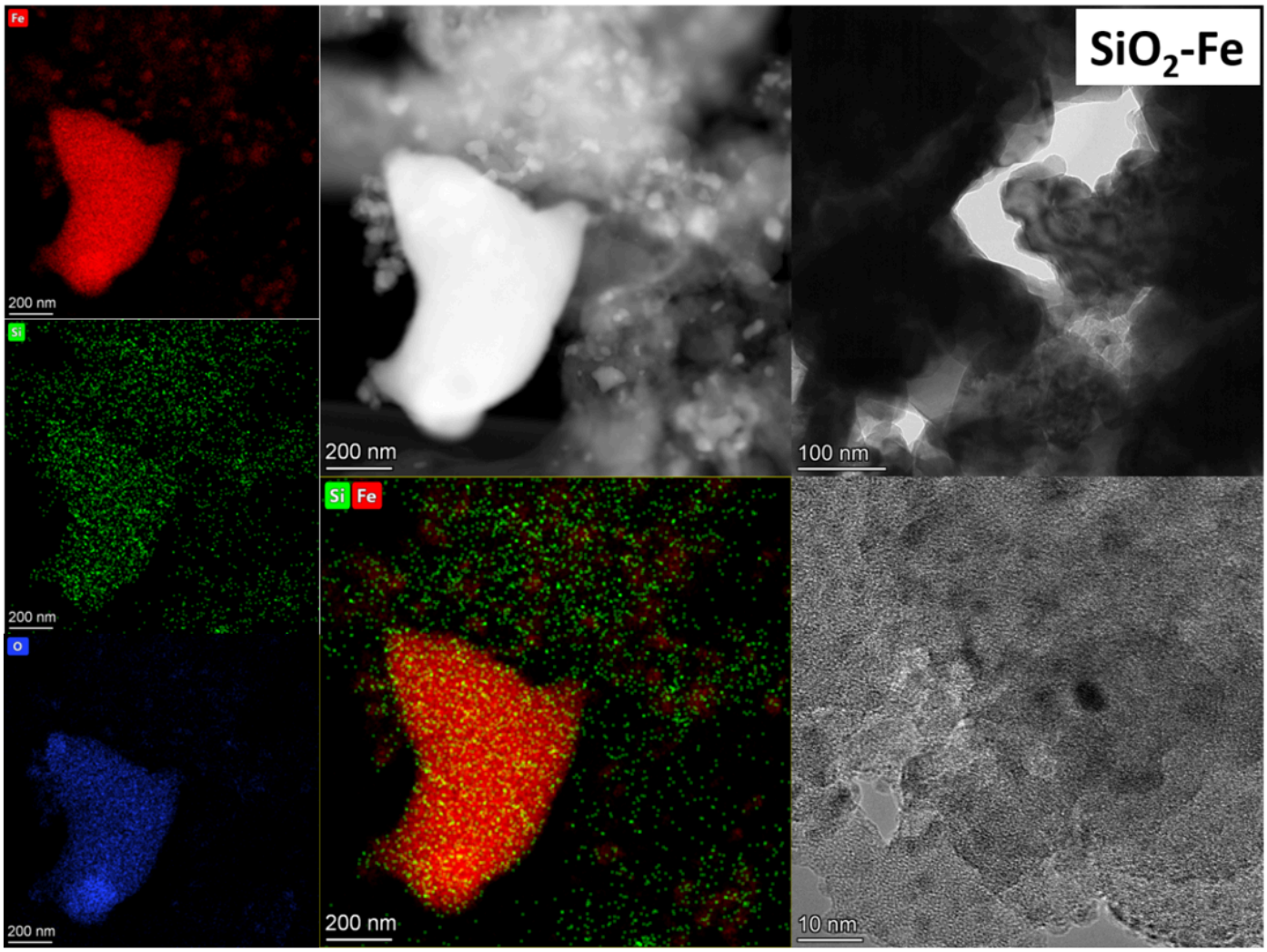



**Figure 4**

TEM, HRTEM, and HAADF-STEM images of $SiO_2$-Fe nanoparticles with EDX elemental maps of Fe (red), Si (green), and O (blue).

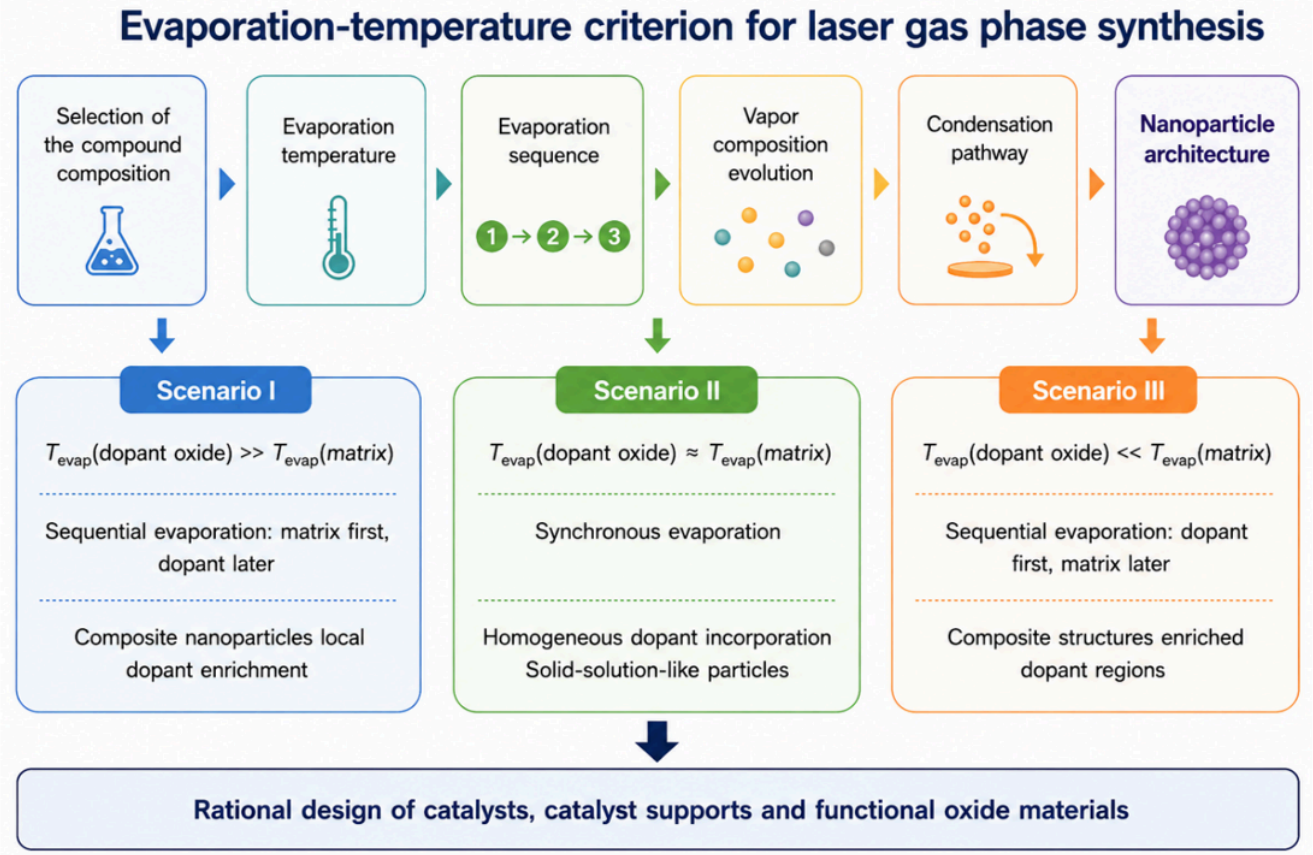



**Figure 5**

Conceptual scheme illustrating the evaporation-temperature criterion for laser gas-phase synthesis of multicomponent oxide nanoparticles at laser intensities below $10^6$ W $cm^{-2}$. The relative evaporation temperatures of the matrix and dopant oxides determine the evaporation sequence, condensation pathway, dopant distribution, and resulting nanoparticle architecture.